# CFD modelling of the cross-flow through normal triangular tube arrays with one tube undergoing forced vibrations or fluidelastic instability.

Beatriz de Pedro[a*], Jorge Parrondo[a], Craig Meskell[b], Jesús Fernández Oro[a]

[a] *School of Engineering, Univeristy of Oviedo, Spain*
[b] *Trinity College Dublin, Ireland*

**Abstract**

A CFD methodology involving structure motion and dynamic re-meshing has been optimized and applied to simulate the unsteady flow through normal triangular cylinder arrays with one single tube undergoing either forced oscillations or self-excited oscillations due to damping-controlled fluidelastic instability. The procedure is based on 2D URANS computations with a commercial CFD code, complemented with user defined functions to incorporate the motion of the vibrating tube. The simulation procedure was applied to several configurations with experimental data available in the literature in order to contrast predictions at different calculation levels. This included static conditions (pressure distribution), forced vibrations (lift delay relative to tube motion) and self-excited vibrations (critical velocity for fluidelastic instability). Besides, the simulation methodology was used to analyze the propagation of perturbations along the cross-flow and, finally, to explore the effect on the critical velocity of the Reynolds number, the pitch-to-diameter ratio and the degrees of freedom of the vibrating cylinder.

*Corresponding author. *E-mail address*: pedrobeatriz@uniovi.es

*Keywords:*
Fluidelastic Instability, Numerical model, Tube arrays, Critical velocity, Disturbance propagation

## 1. Introduction

Cylinder arrays subject to cross-flow such as in shell-and-tube heat exchangers may undergo self-excited vibrations of high amplitude and high potential for structural damage (Weaver and Fitzpatrick (1988); Pettigrew and Taylor (2003a); Pettigrew and Taylor (2003b)). The phenomenon, which is referred to as fluidelastic instability (FEI), can be triggered by either a fluid-damping controlled mechanism, which only requires motion of one tube with one degree of freedom, or a fluid-stiffness controlled mechanism, which requires the coupled motion of several tubes (Chen (1983a); Chen (1983b); Paidoussis and Price (1988)). FEI has been largely studied experimentally in the past, with the main purpose of establishing critical flow velocities as the limiting conditions that ensure stability. However, the data collected of critical velocity for each main geometrical configuration usually show significant scatter. This is attributed to the wide variety of factors with potential to influence the phenomenon, including pitch ratio ($P/d$), number of rows and columns in the array, degrees of freedom, accuracy of cylinder position in the array, details of structural parameters of each cylinder in the array, Reynolds number, turbulence intensity and presence of other excitation mechanisms.

For a given array configuration, a precise estimation of critical veloc-

ity can be obtained by means of the so-called unsteady flow model (Chen (1983a); Chen (1983b)), but it requires the previous determination (usually experimentally) of an extensive set of dynamic force coefficients that represent terms dependent on tube position, velocity and acceleration. These force coefficients are not easy to obtain and are strongly dependent on geometry and reduced velocity. Because of that, several theoretical models have been proposed intended to yield critical conditions for FEI from the estimation of the fluid forces on the tubes, based on different simplifying assumptions (Price (1995)). For instance, the so-called quasi-steady model by Price and Paidoussis (1984) assumes that the fluid-dynamic forces on the tubes can be obtained by performing static flow calculations with a cylinder slightly shifted from equilibrium and then introducing a phase delay for the resulting static forces. Later, Granger and Paidoussis (1996) proposed a more elaborated quasi-unsteady model in which the fluid-dynamic forces are expressed as a combination of transient functions, in order to represent the *memory effect* induced in the flow due to the diffusion and convection of thin vorticity layers from the surface of the vibrating cylinders. Requiring much less empirical input, Lever and Weaver (1986a), developed a semi-analytical model in which the flow passes through the arrays along wavy streamtubes whose cross area fluctuates lagging the motion of the neighboring vibrating cylinders. In this simplified system, the fluid-dynamic forces on the cylinders can be computed by applying the 1D unsteady flow equations (Lever and Weaver (1986b)).

In general, these models capture the essential features of the FEI phe-

nomena up to some extent, but their flow simplifications and the need for empirical data limit their effectiveness as prediction tools. Indeed, the best potential for the detailed description of the flow without empirical data corresponds to CFD models and that capability should allow for more reliable predictions of the critical velocity for FEI. Moreover, CFD offers the possibility of simulating the dynamic response of the flow-structure system even operating at unstable regimes, for which the non-linear terms are dominant. The latter is key to explore possible new situations involving FEI phenomena, such as in the area of fluid kinetic energy conversion.

In recent years, several researchers have applied CFD models to analyze the dynamic flow-structure interaction that leads to FEI. Particular attention has been paid to the case of arrays with only one flexible cylinder undergoing forced vibrations, because it is convenient to study the correlation between tube motion and the associated flow fluctuations. Hassan et al. (2010) used CFD simulations for in-line and normal triangular arrays with one cylinder subject to forced vibration in order to estimate the unsteady force coefficients on the tubes. After verifying good agreement between predicted critical velocities and experimental data, they further investigated the effects of pitch ratio and Reynolds number. This approach was later extended to explore the delay of the perturbations induced in the flow by an oscillating cylinder in a normal triangular array (Hassan and El Bouzidi (2012)) as well as the corresponding fluctuations in the cross-area of the passing streamtubes (El Bouzidi and Hassan (2015)). Khalifa et al. (2013b) performed CFD simulations for a parallel triangular array with one oscillating cylinder, in order

to model the velocity fluctuations previously measured in wind tunnel (Khalifa et al. (2013a)) and to extend their analysis to lower reduced velocities. They obtained good correlation between predictions and measurements, and, besides, they obtained improved estimations of critical velocity when introducing a CFD derived phase lag function in the model by Lever and Weaver (1986a), Lever and Weaver (1986b). Following a different approach, Anderson et al. (2014) developed a simplified numerical model for a small in-line group of cylinders, one of them oscillating, with special focus on the temporal variations induced in the boundary layers and, overall, on the regions of flow attachment and separation. They concluded that the effective time lag between fluid forces and tube motion has two components dependent on flow velocity and vibration amplitude respectively.

In line with these investigations, this paper presents a CFD study on the fluid-dynamic vibrations due to damping-controlled FEI of one single flexible tube in normal triangular arrays. The simulations were developed with the ANSYS-Fluent 12.1 software (ANSYS (2013)). The model incorporates the motion of vibrating cylinders by means of a special User Defined Function, so that the domain is remeshed at every time step. First, the main calculation parameters including boundary conditions and turbulence model were selected by contrasting the predictions of pressure distribution on cylinders with the measurements conducted by Mahon and Meskell (2009) under static conditions. Then, dynamic simulations with one oscillating tube located at the third row were carried out for the sets of configurations tested by Mahon and Meskell (2013) under conditions of forced vibration and by Austermann

and Popp (1995) under conditions of self-excited vibration. This methodology, which pursued the validation of the CFD model at different levels of calculation, is depicted in Fig.1. Finally, simulations were conducted to explore the effects of Reynolds number, pitch ratio and degrees of freedom of the vibrating cylinder.

## 2. CFD Model and Static Calculations

For this study, several normal triangular tube arrays were considered with pitch-to-diameter ratios between 1.25 to 1.58, including the value of 1.32 that Mahon and Meskell (2009, 2013) used in their experiments as well as the values of 1.25 and 1.375 used by Austermann and Popp (1995). In all cases, the array consisted of five rows of six cylinders, as shown in Fig.2. The cylinder diameter was always 38 mm.

Experimental evidence (Austermann and Popp (1995); Khalifa et al. (2012)) indicates that the critical velocity for arrays with one single flexible tube can be very dependent on its location in the array, with the lowest critical velocities generally corresponding to the flexible tube in the third row. According to the study conducted by Khalifa et al. (2012), who collected and analyzed data available in the literature for the main array geometries, that lowest critical velocity for arrays with one flexible tube is very close to the FEI critical velocity for fully flexible arrays. In consequence, for the simulations involving cylinder motion the flexible cylinder was allocated in the third row (tube TV in Fig. 2).

The calculation domain extended both upstream and downstream from the cylinder array with lengths equivalent to nine tube diameters. Preliminary steady flow calculations under static conditions (all cylinders rigid) showed the presence of large scale oscillations in the region downstream the array. While this type of oscillations may actually take place in practice (Olinto et al. (2009); de Paula et al. (2012)), they are not considered to be related to the FEI mechanism. Hassan et al. (2010) also observed this behaviour in their computations and they decided to truncate the domain from the last row of the array as a means to suppress the appearance of those large scale structures. However, this procedure implies imposing boundary conditions (constant outlet pressure) on the flow through the array itself, and that may affect the propagation of disturbances throughout the flow, which is crucial for the development of the FEI phenomenon. In the present model, as an alternative strategy to allow for a reasonable distance between array and domain outlet while preventing large scale oscillations, full-slip guide plates were placed behind each tube of the last row, parallel to main stream (Fig.2).

To discretize the domain, a specially refined grid was used around each cylinder in the array that was composed of quadrilateral cells with an initial thickness of 0.06 mm at the tube wall and a growth factor of 1.15 in the radial direction until the 13th line. This ensured $y^+$ values of the order of 1 for all the simulations conducted. The rest of the domain was meshed with triangular cells of progressively greater size when separating from the array.

In order to prepare the model to deal with cylinder oscillations, a hexagonal region was defined surrounding the vibrating tube (Fig.2), in which the triangular cells could either shrink or expand depending on the instantaneous tube position (Fig.3). On the contrary, the quadrilateral cells attached to the oscillating tube moved without undergoing deformation. This approach meant that, during computations involving cylinder motion, the mesh did not degrade with excessive distortion for cylinder displacements well above 4% of the tube diameter even for the smallest pitch-to-diameter ratio of 1.25 (as shown in Fig.3).

To begin with, a series of computations was performed under static conditions, i.e. no tube vibration. These tests were intended to select the most appropriate calculation parameters when comparing predictions to the wind tunnel data obtained by Mahon and Meskell (2009), who measured the static pressure distribution around the surface of cylinder labeled TV in Fig.2 for the case $P/d$=1.32 and several cross-flow velocities. These pressure data have been non-dimensionalized by defining the pressure coefficient:

$$P^* = \frac{P_s(\theta) - P_{s0}}{\frac{1}{2}\rho U_p^2} + 1 \tag{1}$$

where $P_s$ is the static pressure at location $\theta$ on the tube surface, $P_{s0}$ is the maximum static pressure (at $\theta$=0°), $\rho$ is the fluid density and $U_p$ is the pitch velocity. As an example, Fig.4 compares Mahon and Meskell's experimental data to the predictions obtained for an upstream air velocity of 2 m/s when

using three different turbulence models: a standard $k-\omega$, a $k-\omega$ with shear stress transport corrections ($k-\omega$ SST) and a $k-\epsilon$ with renormalization group ($k-\epsilon$ RNG) complemented with non-equilibrium wall treatment corrections (ANSYS (2013)). They all produce predictions that resemble reasonably well the experimental data, although the standard $k-\omega$ model gives the closest fit in the wake region. This is within expectations since $k-\omega$ models are considered more appropriate than $k-\epsilon$ to deal with separated flow areas, but in the case of closely packed arrays that feature is less relevant than in cases of unconstrained wakes.

On the other hand, the two $k-\omega$ models are seen to be more prone to yield asymmetric predictions of pressure around the cylinders than the $k-\epsilon$ RNG. Different degrees of flow asymmetry depending on the turbulence model can be also observed in the computations reported by Iacovides et al. (2014), who used detailed LES simulations of the flow across an in-line square array to contrast the predictions from RANS simulations with five different turbulence models. Interestingly, the predictions closest to the LES results, which gave an asymmetric distribution, corresponded to the $k-\epsilon$ model in that study. Since the FEI phenomenon is usually associated to vibrations in the transverse direction, it is key to estimate accurately the lift forces and they are mostly influenced by the pressure unbalance at the regions around $\Theta = 90^{\circ}$ and $\Theta = 270^{\circ}$ (Fig. 4), where pressure is minimum. According to this criterion the $k-\epsilon$ RNG model was selected for the subsequent computations.

Another computation series explored the effect of the type of boundary condition at the channel sides downstream of the array. Specifically, first they were modeled as full-slip walls and secondly as planes with periodic repetition of the flow variables. Fig.5 shows the respective pressure distributions around three reference cylinders of the third row, labeled as TV, T7 and T8 in Fig.2. Again, some degree of flow asymmetry can be expected during the iteration process between different cylinders even if they belong to the same row. The periodic boundary condition is not really symmetrical since it imposes continuity in the derivatives of the flow variables across the boundary. Despite this, in the present case it was seen to produce the most symmetrical flow in the domain (Fig.5b), with pressure distributions around the three cylinders that are almost identical. This can be attributed to the less rigid restrictions imposed on the flow by the periodic boundaries (for instance, they allow through-flow), which favor the attenuation of possible symmetrical disturbances formed during the computational process downstream the half cylinders at the channel sides. In consequence the boundary conditions at the channel sides were defined as periodic for the rest of cases tested. This symmetric pattern for the stream can also be appreciated in Fig.6, which shows typical contours of velocity magnitude and static pressure obtained from steady flow simulations.

Finally, the effect of cell size was analyzed by comparing the fluid forces computed for meshes with four different refinement degrees. Each mesh was characterized by the number of cells adjacent to each tube along its perimeter, which varied between 100 and 250. In particular the reference magnitudes

considered for contrast were the derivative of the lift coefficient on tube TV (Fig.2) with respect to its transverse position and the drag coefficient at neutral position, which are the relevant parameters used in the quasi-steady theory by Price and Paidoussis (1984). In each case, the derivative of the lift coefficient was estimated by applying a first order central difference scheme from calculated lift force data on tube TV when it was held apart from its neutral position at $\pm 0.5\%$ of tube diameter in the transverse direction. Fig.7 shows the results obtained for the array of $P/d = 1.25$, expressed in values relative to the data for the most refined mesh. It is seen that above 150 nodes per tube mesh the differences both in drag and lift derivative are reasonably small. The bulk of the simulations reported in this paper corresponds to the mesh with 200 nodes/tube, for which the difference with respect to the 250 nodes/tube mesh was less than 1.6% for the lift derivative and 0.06% for the drag. The corresponding total number of cells in the domain ranged from $2.8 \times 10^5$ for $P/d = 1.25$ to $4 \times 10^5$ for $P/d$=1.58.

## 3. Forced oscillations in the transverse direction

### *3.1. Flow fluctuations*

The first series of dynamic simulations corresponded to the case of tube TV in motion under harmonic forced oscillation in the transverse direction, in order to explore the transmission of perturbations along the air stream through the array. For that purpose, a special routine (User Defined Function, ANSYS (2013)) was coupled to the CFD code so that the tube position and velocity, as well as the domain grid, could be conveniently updated at

every time step during calculations. In addition, fifteen points were selected along a stream channel that passes by tube TV (Fig.8), in order to monitor their velocity vector and pressure during computations. Of them, positions e-k are distributed in the region adjacent to tube TV at a radial distance between 5% (point h) and 12% (e and k) of tube diameter (relative to the equilibrium position). The other nodes are located at similar positions with respect to the preceding and posterior cylinders (T1 and T3). Each of these nodes is associated to a linear coordinate S along the stream, with S=0 at node h (Fig.8). For these simulations the time step was set to 0.5 ms, which corresponds to 256 steps per oscillation. This time step was considered small enough to not affect the results since the steps/cycle are about three times higher than the values recommended by Hassan et al. (2010) for equivalent simulations under forced vibrations.

- *Flow distribution at maximum displacement*

Fig.9 shows the calculated contours of velocity, vorticity and static pressure ($P/d$=1.25, $d$=38mm, $U_0$=1.26 m/s) in the region surrounding the vibrating tube (at 7.81 Hz) at the instant of maximum tube displacement (3% of tube diameter towards the top side of the image). The general velocity pattern (Fig.9 a) correlates well with the visualization picture obtained for a normal triangular tube array with P/d =1.5 by Scott (1987) (reported in Khalifa et al. (2012)). It clearly shows how the main stream of air detaches from each cylinder (T1, T4, TV) and, after an inflexion region at a somewhat lower velocity, reattaches to the next one. The main stream flows along channels or streamtubes that resemble the ideal pattern depicted by Yetisir

and Weaver (1993a), Yetisir and Weaver (1993b) for staggered arrays, though the velocity in those channels is far from uniform. Compared to the modified pattern used by El Bouzidi and Hassan (2015), the present computations support excluding a small stagnation zone on the front of the tubes, but their definition of a rather narrow wake region is less justified.

The flow dettachment can also be noticed in the vorticity map (Fig. 9b), which highlights the positions with high velocity gradients. Maximum vorticity values are located on the boundary layers along the tubes, which eventually result in flow separation. The latter is characterized by two tongue-like vorticity projections from the rear of the tubes, one at each side, representing the transition between wake and main stream. Granger and Paidoussis (1996) consider the diffusion and convection of these thin vorticity layers as the origin for the lag of the fluid forces with respect to cylinder motion. Finally, pressure (Fig. 9c) is seen to be lowest in the gap region between cylinders of the same row, where velocity is highest, and is high at the stagnation zone on the front of each cylinder (TV, T3, T6) as well as in the wakes (T1, T4, TV).

Comparing the upper and lower halves of the maps of Fig. 9 reveals asymmetries that are due to the shifted position of tube TV from equilibrium and to the time lag with which the flow accommodates to the tube motion. The latter produces a kind of waving flag effect at the border of the wakes from the oscillating tube and the fixed cylinders. At the instant of Fig. 9, the separation between tubes TV and T5 is lowest while it is largest between TV and

T2. Because of that, the flow passing between cylinders T1 and T4 deviates down at higher rate than up, and so the velocity of the main stream through tubes TV and T1 is higher than through TV and T4. Also, the wake from T4 has swelled until nearly merging with the stagnation zone on TV, creating a relatively large area at high pressure. However, despite the higher flow-rate below tube TV than above it, the average velocity at the gap between TV and T2 is lower than between TV and T5 (the opposite regarding average pressure), i.e. the flow-rate distribution has not yet reached proportionality to the gap size. Downwards, the passage between TV and T3 is analogous to the region between TV and T1, whereas the passage between TV and T6 resembles the region between TV and T4, including the wake swelling effect toward the stagnation zone on tube T6 despite the low average pressure on top of tube TV.

• *Velocity fluctuations*

Fig.10 shows the normalized amplitude and phase of the velocity fluctuations at 7.8 Hz computed at each node for upstream velocities $U_0$= 0.63, 1.26 and 1.89 m/s (reduced pitch velocity $U_r$=10.6, 21.2 and 31.8; pitch Reynolds number Re= $8 \times 10^3$, $1.6 \times 10^4$ and $2.4 \times 10^4$). Despite the range covered, the three amplitude curves are very similar. This can be attributed to the low value of the cylinder velocity with respect to the cross stream and, also, it indicates little dependence on the Reynolds number. Node c exhibits the most noticeable effect of flow velocity variation: its velocity amplitude decays fast when increasing the flow velocity because this provokes the wake of tube T1 stretch downstream so that node c gets out progressively from the

wake border into the main stream. As expected, far from the vibrating tube the velocity amplitude decreases both up and downstream, with nearly no fluctuation at node a. However, the velocity amplitude is also low between nodes f and h, despite being close to the position of maximum channel constriction and enlargement when the cylinder vibrates. Highest fluctuations correspond to nodes c-e and, overall, i-m, which represent locations near the regions of flow separation from tubes T1 and TV respectively. Hence, they can be attributed to the wake oscillations lagging the motion of tube TV. The formation of disturbances at these regions is consistent with the memory effect that Granger and Paidoussis (1996) described due to the diffusion and convection of thin vorticity layers from the oscillating tube surface. These vorticity layers have been highlighted in the vorticity map of Fig. 9b. Despite tube TV oscillates only in the y-direction, the velocity fluctuations are considerably higher in the x-direction, except for nodes a-c.

These predictions can be compared to the computations performed by Hassan and El Bouzidi (2012) for a normal triangular array with $P/d$=1.35, who focused in the propagation upstream of the disturbances induced by an oscillating cylinder at the fourth row, under a range of flow velocity and Reynolds number. Like in the present study, their predictions were little dependent on the reduced velocity, unless it had very low values. For reduced velocities in the range of the current tests, their data showed that the amplitude of velocity fluctuations gets a minimum close to zero at a position approximately equivalent to node g, in line with the current predictions. However, further upstream their data showed a relatively constant amplitude

of about $0.02 \times U_0$ until approaching the preceding cylinder, i.e. they did not predict any high fluctuations in the region of nodes c-d as in the present study. It is unclear whether this difference between predictions is due to a different selection of reference nodes or to different values for the parameters of the system (like $P/d$).

Regarding the velocity phase (Fig. 10b) at the nodes with high amplitude, from c to e the phase is close to 0°, i.e., its velocity is approximately in phase with the motion of TV, whereas at node j (where amplitude is maximum) the phase is about 25°-30°. From node j to o the phase increases quite progressively up to about 60° for the smallest flow velocity. This confirms that in the stream channels between T1 and TV and between TV and T3, the instantaneous flow-rate is close to highest when tube TV is at top position. On the contrary, the velocity phase at node h is about 105°-115°, thus confirming that the increment in flow-rate below TV when it is at top position is partially counterbalanced by the increment in cross-section between TV and T2 (as previously deduced from Fig. 9a). Again, these predictions differ substantially from the phase data computed by Hassan and El Bouzidi (2012), who reported relatively constant values upstream (at about 190°) and downstream (at about 140°) whereas the phase got a deep minimum in the vicinity of s$\sim$ 0.

Besides, Fig. 10b shows that the slope of the phase progression from node j to o is dependent on the reduced velocity $U_r$, the higher $U_r$ the lower the slope. This suggests that the velocity disturbances induced by TV travel

downstream at a propagation speed that increases with $U_r$. For any given $U_r$, the phase curve is slightly less steep (i.e. faster propagation) before node l. This is so because nodes j-k are right in the area of disturbance formation (wake border close to separation point) and so they are affected very directly by the oscillations of tube TV. Table 1 presents the propagation speed estimated after performing a linear fit of the phase data for the last four nodes l-o, each at its curvilinear coordinate $S$. For the three cases, the determination coefficient $R^2$ is above 0.985. The ratio between the disturbance propagation speed and the gap velocity is seen to take values between 0.8 for $U_r$=31.83 and 0.88 for $U_r$=10.61, i.e. it reduces just 10% in spite of tripling $U_r$.

| $U_r$ | $U_g$ (m/s) | $V_d$ (m/s) | $R^2$ | $V_d/U_g$ |
|---|---|---|---|---|
| 10.61 | 3.15 | 2.76 | 0.997 | 0.88 |
| 21.22 | 6.30 | 5.29 | 0.986 | 0.84 |
| 31.83 | 9.45 | 7.59 | 0.986 | 0.80 |

Table 1: Propagation velocities $V_d$ of the disturbances downstream the flow detachment region of tube TV.

These results can also be compared to the findings by Khalifa et al. (2013a) based on hot-wire measurements in the cross-flow through a parallel triangular array with $P/d$=1.54. Like in the present study, they identified the region of flow detachment from the vibrating cylinder as the source for flow disturbance propagation, which is in line with Granger and Paidoussis (1996) explanation for the flow memory effect. Besides, Khalifa et al. (2013a)

observed that the propagation speed downstream was proportional to the gap velocity, with a factor of about 0.52. Certainly, the higher value of this factor in the present study can be attributed to the different array configurations regarding both $P/d$ (1.25 instead of 1.54) and geometry (normal triangular instead of parallel triangular): the parallel triangular has well defined stream lanes, while the flow through a normal triangular array follows a more tortuous route, so that when a tube is displaced, there can be flow crossing from one lane to the next.

Khalifa et al. (2013a) also observed clear propagation upstream, at a speed about 20% lower than downstream. This is not so in the present study probably because of the array geometry: the oscillations of tube TV also induce significant oscillations in the wakes from upstream tubes T1 and T4, so that their wake borders can be considered as secondary disturbance sources that interfere with the main perturbations from tube TV. According to these results, considering a constant speed for the disturbance propagation through normal triangular arrays, which is in line with the usual assumptions in Lever and Weaver's theory (1986a,b), would be reasonable for propagation downstream from the vibrating cylinder. However, it appears to be too simplistic for propagation upstream, i.e. a more complex propagation model would be required for this case.

Finally, the results presented in Fig. 10 indicate very little dependence on the reduced velocity in the range of the tests, but that independence is not expected to stand for lower reduced velocities as observed in the com-

putations by Hassan and El Bouzidi (2012) for a normal triangular array and Khalifa et al. (2013b) for a parallel triangular array. In particular, the latter obtained that the velocity phase when reducing the flow velocity to very small values evolves to a state of 0° upstream and 180° downstream, with a sharp change at the coordinate $S$=0.

- *Pressure fluctuations*

Fig.11 shows the static pressure fluctuations in amplitude and phase (relative to the position of tube TV). These pressure fluctuations are the consequence of the kinetic energy variations along the flow and the corresponding local accelerations (fluid inertia) as the flow adapts to the cylinder oscillations. Now highest fluctuations are seen to correspond to nodes h-j for the three flow velocities tested. That is the zone where flow decelerates while detaching from the oscillating tube, again in line with Granger and Paidoussis (1996). In fact, the pressure pattern of Fig. 11 resembles reasonably closely the pressure measurements performed around a vibrating cylinder by Mahon and Meskell (2009) for a similar array (normal triangular, $P/d$=1.32), including the pressure dip at node i ($S/d$=+0.25).

Considering the pressure phase, there is a minimum at node i that gets deeper for increasing values of $U_r$, while in the neighbour nodes (h, j, k) fluctuations are seen to be approximately in phase with the motion of tube TV, i.e. pressure there is highest when tube TV is at the top position as in Fig.9c. This is so because, at that instant, the local cross-section is largest and so the stream velocity is lowest, and, besides, the wake is well separated

from nodes j-k and the stagnation region on cylinder T3 is growing towards tube TV. For that situation, the flow-rate along the monitored lane is close to highest because of the enlarged cross-section at h-j. This increases the velocity downstream (l-o) while pressure there reduces to a minimum. For that reason, the pressure phase shifts about 180° from k to l for the three flow velocities tested. Upstream, the pressure phase also evolves towards values in the range of 180° at nodes a-b, but the progression is quite different depending on the flow velocity. For the lowest Ur the variation in pressure phase is smoother, though there is some ridge at e-f that is related to the oscillations of the wake from the precedent cylinder T1. Increasing Ur, however, results in another 180° shift near node g, at which the pressure amplitude reduces almost to zero.

### *3.2. Delay of lift force*

A second series of computations were focused on the time delay of the fluid-dynamic force applied on the oscillating tube during its motion, which is key in the development of damping-controlled FEI. In particular, these computations were designed to reproduce the conditions of the experimental study by Mahon and Meskell (2013), who used a normal triangular array with $P/d = 1.32$ and $d = 38$ mm in which a single cylinder at the third row could be forced to vibrate transversely while subject to air cross-flow. They measured the time delay between lift and tube acceleration for upstream velocities from 2 to 10 m/s, which gives reduced pitch velocities from 25.4 to 127.6 and Reynolds numbers from $2.2 \times 10^4$ to $11.2 \times 10^4$ (based on pitch velocity). Present simulations were conducted for that velocity range with

tube TV (Fig. 2) oscillating at 8.6 Hz and amplitude of 1% of tube diameter, in correspondence with some of Mahon and Meskellś experiments.

The predictions obtained of time delay $\tau$ between lift and tube acceleration have been normalized by the residence time $d/U_p$, yielding a retardation parameter $\mu$ (Eq. 2):

$$\mu = \frac{\tau U_p}{d} \tag{2}$$

This retardation parameter is similar to the one introduced by Price and Paidoussis (1984) in their quasi-steady model, though the conditions assumed for that theory (linear lift forces derived from steady flow tests on arrays with one statically shifted tube) are very different from the current dynamic tests. In the latter case, fluid forces are expected to contain both stiffness and damping components, i.e. they are related not only to tube position but also to tube velocity. In fact, Meskell and Fitzpatrick (2003) determined experimentally those two components for the same array of the current tests under a variety of flow velocities, revealing the non-linear character of the damping term.

Fig. 12 shows the calculated retardation parameter as a function of air flow velocity. It also includes the experimental values corresponding to Mahon and Meskell's tests (2013) for vibrations at 8.6 Hz, after normalizing their reported data with pitch velocity instead of upstream velocity. For low velocities, there is a significant discrepancy between predictions and measurements: the measured values lay between 1.2 and 1.4, whereas predictions

give values for $\mu$ well above 2, with a maximum of 2.32 at $U_r \sim 50$. For higher air flow velocities, the predicted $\mu$ reduces progressively with final values in the order of 1, suggesting some further reduction of $\mu$ for air velocities above the upper limit of the tests. The experimental data are somewhat scatter, but they also denote a decaying trend for $\mu$ in the upper range of air velocities tested. In fact, the agreement between predictions and measurements is remarkable for $U_r > 70$.

Considered as a whole, Mahon and Meskell's data indicate little variation of $\mu$ with the air flow velocity, with an average value of $\mu$=1.3. Indeed, this value is in very good agreement with Price and Paidoussis's suggestion of $\mu \sim O(1)$ (1984), despite the different conditions mentioned above between the quasi-steady theory and the current dynamic tests. Besides, that value is in line with the predictions now obtained except for the low range of flow velocities tested ($U_r < 70$). Here, the high values predicted for $\mu$ indicate an excessive ratio between the force delay and the residence time associated to the main stream, the latter being inversely proportional to the air velocity (Eq. 2). This means that if, for instance, the reduced velocity were halved from $U_r = 80$ to $U_r = 40$, the time delay of the fluid-dynamic force would be doubled under a constant $\mu$ basis, whereas current predictions would give an increment by a factor of 3. The reason for the discrepancy between $\mu$ predictions and Mahon and Meskell's data for the low range of flow velocities is uncertain. Nonetheless, the agreement achieved for $U_r > 70$ was satisfactory enough to justify further exploration on new dynamic tests, as described in the next section.

## 4. Self-excited vibrations

For the simulations reported in this section, the user defined function that governs the motion of the vibrating tube was modified to incorporate the computed instantaneous fluid-dynamic forces in the tube motion equation (Eq. 3), considered as a single degree-of-freedom system in the transverse direction:

$$F(\ddot{y}, \dot{y}, y, U_0)_y = m_s\ddot{y} + c_s\dot{y} + k_s y = F_y(t) \tag{3}$$

This means that the only movable tube of the array (TV in Fig. 2) was prevented to shift streamwise due to drag, so that the array pattern did not become distorted. The new user defined function allowed that, at each time step, the tube position and grid were updated after using a discretized version of Eq. (3) (derivatives approximated by finite difference ratios) to determine the new instantaneous tube velocity based on a second-order backward scheme.

The typical simulation procedure began with a pre-calculation for steady flow and all cylinders static, in order to establish appropriate initial conditions for the dynamic calculations. Then the dynamic simulation for unsteady flow was launched, i.e. tube TV (Fig. 2) was set free to move according to the fluid forces computed at each time step. Since the starting flow was never perfectly symmetrical, the initial lift force was non-zero and this triggered the oscillation of tube TV about its equilibrium position (displaced about $10^{-3} \times d$). As expected for air cross-flow, the added mass effects were

small and the oscillations took place at the tube natural frequency as defined by its mass $m_s$ and rigidity $k_s$. Depending on the cross flow velocity, the vibration amplitude could either decay or amplify (Fig. 13). In the first case the net damping of the system is positive and so the system is stable, whereas in the second case the net damping is negative and the system is dynamically unstable. The latter corresponds to damping controlled fluidelastic instability.

The damping of the system can be estimated by monitoring the tube motion and analyzing the amplitude decay (or growth). It was noticed that the resulting damping coefficient might be distorted depending on the time step. In consequence, preliminary simulations were undertaken to explore that effect for the reference case of $P/d$=1.25, natural frequency $f_n$= 9.42 Hz and mass-damping parameter $m_r\delta$ = 26.7. The cross-flow had an upstream velocity of 1.58 m/s, for which this reference case is unstable. Fig. 14 compares the predictions obtained for six time steps from $\Delta t$=0.7 to $\Delta t$=0.1 ms, with the damping values normalized by the damping with $\Delta t$=0.1 ms. As expected, the predictions show very little variation for sufficiently small values of the time step, approximately below 0.2 ms. All subsequent simulations were conducted with a time step of $\Delta t$=0.15 ms, for which the relative deviation against the damping with $\Delta t$=0.1 ms was 0.13%. This gives about 700 steps per oscillation, which is considerably higher than the steps/cycle used in other studies (Hassan et al. (2010)).

Fig. 15 shows the time evolution of the tube vibration amplitude as ob-

tained from the envelope curves of the tube response for the case $P/d$=1.25 and $m_r\delta$=18.7, when subjected to six cross-flows with velocity ranging from $U_0$=0.89 m/s to $U_0$=1.17 m/s. At low velocity the slope of the curves is negative, thus indicating that the net damping is positive and so the system is stable. Increasing the flow velocity makes the slope more horizontal, i.e. the damping coefficient gets smaller, until a velocity at which the slope turns positive and so the damping becomes negative and the system can said to be unstable. That velocity represents the critical threshold for fluidelastic instability.

This method for delimiting the critical velocity was put into practice for the cases tested in wind tunnel by Austermann and Popp (1995), who used arrays with $P/d$=1.25 and $P/d$=1.375 in which a single tube located at the third row (like tube TV in Fig. 2) oscillated only in the transverse direction (tube diameter $d$=38 mm, natural frequency $f_n$=9.42 Hz). In fact, that tube was prevented to shift downstream, as the tube equilibrium position was corrected by adjusting the mounts of the cylinder with a computer controlled system. This arrangement is thus equivalent to a single-degree-of-freedom as assumed for the CFD simulations reported in this section. By means of a precise regulation of the damping of that tube, Austermann and Popp obtained very accurate data of critical velocity for ranges of the mass-damping parameter from 11 to 70 for $P/d$=1.25, and from 11 to 42 for $P/d$=1.375.

For the simulations, the cross-flow velocity was progressively increased at intervals equivalent to 5% of the experimental critical value. Fig.16 compares

Austermann and Popp's data of reduced critical velocity to the current CFD predictions, represented by the highest $U_r$ tested that showed stable regime behavior and the lowest $U_r$ that showed unstable regime. The relevant data is collected in Tables 2 and 3. It is observed that, though the predictions underestimate the experimental critical velocities almost systematically, in most cases it is only by about 5-10%. Hence, the simulation procedure can be regarded to give reasonable conservative estimates of the critical velocity for FEI, and this justifies applying the method to explore the effect of different system parameters, as reported in the next section.

| $m_r\delta$ | CFD highest stable $U_r$ | CFD lowest unstable $U_r$ | Experimental $U_{cr}$ | Relative difference (%) |
|---|---|---|---|---|
| 11.42 | 10.61 | 11.32 | 14.15 | $-20\% \Leftrightarrow -25\%$ |
| 14.60 | 12.03 | 12.73 | 14.15 | $-10\% \Leftrightarrow -15\%$ |
| 18.67 | 13.22 | 14.00 | 15.55 | $-10\% \Leftrightarrow -15\%$ |
| 22.68 | 14.91 | 15.74 | 16.56 | $-5\% \Leftrightarrow -10\%$ |
| 26.71 | 15.88 | 16.76 | 17.64 | $-5\% \Leftrightarrow -10\%$ |
| 29.59 | 16.91 | 17.85 | 18.79 | $-5\% \Leftrightarrow -10\%$ |
| 34.50 | 19.19 | 20.25 | 21.32 | $-5\% \Leftrightarrow -10\%$ |
| 39.81 | 20.44 | 21.57 | 22.71 | $-5\% \Leftrightarrow -10\%$ |
| 49.36 | 23.18 | 24.47 | 25.76 | $-5\% \Leftrightarrow -10\%$ |
| 59.34 | 27.44 | 28.81 | 27.44 | $0\% \Leftrightarrow 5\%$ |
| 69.18 | 29.08 | 30.80 | 34.22 | $-10\% \Leftrightarrow -15\%$ |

Table 2: Comparison of predicted critical velocity and experimental data from Austermann and Popp (1995) for the P/d=1.25 tube array.

| $m_r\delta$ | CFD highest stable $U_r$ | CFD lowest unstable $U_r$ | Experimental $U_{cr}$ | Relative difference (%) |
|---|---|---|---|---|
| 11.48 | 13.36 | 14.10 | 14.84 | $-5\% \Leftrightarrow -10\%$ |
| 18.50 | 14.95 | 15.88 | 18.68 | $-15\% \Leftrightarrow -20\%$ |
| 25.17 | 17.64 | 18.82 | 23.52 | $-20\% \Leftrightarrow -25\%$ |
| 33.17 | 27.54 | 29.07 | 30.60 | $-5\% \Leftrightarrow -10\%$ |
| 42.34 | 33.84 | 35.83 | 39.81 | $-10\% \Leftrightarrow -15\%$ |

Table 3: Comparison of predicted critical velocity and experimental data from Austermann and Popp (1995) for the P/d=1.375 tube array.

## 5. Effect of system parameters

### *5.1. Reynolds number*

It was considered the reference case of $P/d$=1.25 and $m_r\delta = 26.7$ subject to air cross-flow ($\upsilon = 1.51 \times 10^{-5}\ m^2/s$), which corresponds to one of the experimental data by Austermann and Popp (1995). For this case, the Reynolds number based on tube diameter ($d$=38mm) and gap velocity at experimental critical conditions ($U_g$=6.3 m/s) was $Re = 1.6 \times 10^4$. Again, simulations were carried out for successive flow velocity increments of 5% of the experimental critical value, but now the fluid viscosity was increased accordingly, so that the Reynolds number did not change. This procedure of viscosity adaptation was repeated for four higher Reynolds numbers, up to $10^5$. The results are presented in Fig.17. It is seen that the critical velocity for FEI, as delimited by the highest $U_r$ in stable regime and the lowest $U_r$ in unstable regime, increases by about 20% within the range of Reynolds numbers tested, with a slope progressively steeper when approaching the upper

limit of $Re = 10^5$.

This moderate influence of $Re$ is consistent with the study by Charreton et al. (2015), who collected data from the literature of lift coefficients on statically displaced cylinder for relatively high values of $Re$. On the contrary the effect of $Re$ below 200, as obtained by these researchers from both computations and experiments on a parallel triangular array, was very strong. Besides, the trend of increasing $U_r$ for higher $Re$ is consistent with specific experimental studies (Chen and Jendrzjczyk (1981); Mewes and Stockmeier (1991)) and with the high and scattered values of the critical velocity usually observed in practice for arrays subjected to intensely turbulent flows (Weaver and Fitzpatrick (1988); Au-Yang et al. (1991); Pettigrew and Taylor (2003a)). That scatter, with variations in critical velocity well above 20%, might be related to an increasing slope of $U_r$ at $Re \sim 10^5$ as obtained in the current study, which suggests still further increments of critical velocity with $Re$.

From the current simulations, the predictions under controlled moderate Reynolds number conditions ($Re \sim 10^4$) might be considered as an appropriate low-bound estimation for the critical velocity in practice. However, further research would be required to characterize the conditions in which that result can be extended to other configurations. For instance, in case of two-phase flow the effect of $Re$ can be totally masked, as deduced from the measurements by Sawadogo and Mureithi (2013) of the fluid forces on a statically displaced cylinder in a parallel triangular array subjected to two-phase

cross-flow with different void fractions.

*5.2. Pitch ratio*

Starting again from the reference conditions of $P/d$=1.25, $m_r\delta$ = 26.7 and air cross-flow, the previous simulation procedure was now applied on four new arrays with successively greater pitch ratios, up to 1.58. Now the fluid viscosity was kept constant, so $Re$ varied proportionally to the air velocity. The results are presented in Fig.18. From $P/d$=1.25 to 1.375 the critical velocity is seen to increase about 10%, whereas for higher $P/d$ values the effect appears to be much smaller. In fact, the trend becomes uncertain because the variations observed are of the order of the increments in stream velocity between consecutive simulations for a given $P/d$.

The increment of critical velocity with tube spacing is in agreement with the results from different experiments and theoretical models (citeprice95). In particular the results obtained are consistent with the predictions reported by Hassan et al. (2010) for normal triangular arrays when changing $P/d$ from 1.35 to 1.75, which gave values for $U_r$ about 20% higher. However a further increment to $P/d$=2.5 produced a much higher variation in $U_c$, well above 50%.

The current results suggest defining a limit $P/d$ whose critical velocity would be a reasonable estimate of critical velocities for higher pitch ratios, at least up to the highest p/d value now tested. For the particular conditions of these tests (normal triangular arrays, one flexible tube with a 1DOF, $m_r\delta$ in the order of 25-30) that limit $P/d$ value could be laid in the interval 1.3-1.35.

On the contrary lower pitch ratios would require specific estimations of the corresponding critical velocity. According to this, engineering design criteria that do not include the effect of pitch ratio, as is usually the case (Au-Yang et al. (1991)), might give unconservative estimations of critical velocity for very low $P/d$ values. These conclusions derive from numerical tests for a very specific configuration, so further research would be required to extend them to other cases.

*5.3. Degrees of freedom*

Up to this point, the motion of the vibrating tube TV was restricted to the transverse direction, but now the user defined function was modified to relax that condition and allow motion in the streamwise direction as well. The motion equations considered for the two-degree-of-freedom (2DOF) tube were:

$$F(\ddot{x}, \dot{x}, x, U_0)_x = m_s\ddot{x} + c_s\dot{x} + k_s x = F(t)_x \tag{4}$$

$$F(\ddot{y}, \dot{y}, y, U_0)_y = m_s\ddot{y} + c_s\dot{y} + k_s y = F(t)_y \tag{5}$$

with identical values of mass and structural damping and rigidity in both orthogonal directions. Fig.19 shows a typical trajectory of tube TV after switching from the initial static conditions to full dynamic simulations. Since the drag force on the tube is non-zero, first the tube crosses some distance downstream, further than the new equilibrium position ($\Delta x = O \sim 10^{-2}d$). Since there is also some unbalance in the transverse direction, tube TV undergoes oscillations both streamwise and transversely to the main stream, thus composing an orbital motion. However, the amplitude of the stream-

wise oscillation decays rapidly, and very quickly the remaining vibrations take place mostly in the transverse direction, like a 1DOF system. Again, these transverse oscillations can either reduce or increase along time, as is the case in Fig.19. The former corresponds to stable regime and the latter to unstable, i.e. to damping-controlled FEI.

Another series of simulations was conducted to estimate the critical velocity corresponding to $P/d$=1.25 over the range of $m_r\delta$ tested by Austermann and Popp but now with two degrees of freedom allowed for tube TV. The fluid viscosity was kept constant so that $Re$ varied accordingly to flow velocity. Because of the 2DOF, the equilibrium position of TV became shifted downstream approximately between 1% and 5% of the inter-cylinder gap for the range of cross-velocities tested. Fig.20 shows the new predictions, along with the experimental data of Andjelic (1988) for $m_r\delta$=11.42 (reported in Austermann and Popp (1995)). He determined the critical velocity with the same experimental set up of Austermann and Popp (1995) but without any means to correct variations in the equilibrium position due to drag. Therefore, his configuration was equivalent to the current 2DOF simulations. The most noticeable effect is the drop from the previous predicted critical velocities in about 25% for low $m_r\delta$, which increases to 30% for high $m_r\delta$. This drop is similar to the experimental difference between the critical velocity of Austermann and Popp (1995) (see Fig. 16a) for the corrected geometry, and the single point determined by Andjelic (1988) for the case with the shifted cylinder. Certainly, more experimental data would be required to achieve an adequate support for these predictions.

According to them, small variations in the equilibrium position of the flexible tube can affect significantly the critical velocity for damping-controlled instability. In particular, the estimations for normal triangular arrays of low $P/d$ with a 1DOF flexible tube can be unconservative by 25-30% if compared to the case of a small shift downstream for that tube. In consequence, though the instability is still associated to oscillations in the transverse direction, simulations intended to estimate FEI thresholds should also allow for cylinder displacement streamwise.

A separate issue is whether these critical velocities for arrays with a 2DOF flexible tube are representative of the critical conditions for fully flexible arrays. Khalifa et al. (2012) studied the critical velocities under both situations by selecting data from the literature for the main array geometries and from a new experimental study on a parallel triangular array. The collected data is scant and sparse and no data was finally provided for the normal triangular geometry. However, the general trend suggests that critical velocities for fully flexible arrays and for arrays with one single flexible tube can be very similar provided the flexible tube is located at a specific row that gives the lowest critical velocity. According to the study by Austermann and Popp (1995), for normal triangular arrays with $P/d$=1.25 that lowest critical velocity would correspond to the flexible tube located in the third row, like in the present study.

## 6. Conclusions

A CFD methodology involving structure motion and dynamic re-meshing has been put into practice to simulate the self-excited vibrations due to damping-controlled fluidelastic instability in a normal triangular cylinder array with a single flexible tube located in the third row. URANS 2D computations were performed with the commercial code Fluent 12.1 complemented with user defined functions to account for the flexible tube motion. Appropriate model parameters regarding mesh refinement, boundary conditions, turbulence model and time step were selected by comparing calculations to experimental data under static conditions (Mahon and Meskell (2009)) as well as to ensure minimum influence on predictions. In particular, large-scale disturbances downstream the array were avoided by using parallel guide plates instead of truncating the computation domain at the last row like in other precedent models.

This CFD methodology was contrasted by comparing predictions to experimental data reported in the literature regarding i) time lag of lift coefficient under transverse forced vibrations with $P/d$=1.32 (Mahon and Meskell (2013)) and ii) critical velocity for 1DOF FEI with $P/d$=1.25 and $P/d$=1.375 over a range of the mass-damping parameter (Austermann and Popp (1995)).

In the case of lift lag under forced vibration, the predictions obtained for the retardation parameter $\mu$ were in remarkable agreement with Mahon and Meskell's measurements for reduced pitch velocities in the range 70-130, denoting a decaying trend for $\mu$. However, in the range 25-65 the predictions

of $\mu$ were excessively high in about 75%. The average value of Mahon and Meskell's data is $\mu$=1.3, which is notoriously in line with Price and Paidoussis (1984) suggestion of $\mu$=$O \sim (1)$ (1984), despite the different conditions between the quasi-steady theory and the current dynamic tests.

Besides, the analysis of the velocity and pressure fluctuations along the stream suggests that the main flow disturbances originate in the region of flow detachment from the vibrating tube, in line with Granger and Paidoussis (1996) explanation for the flow memory effect and with the experimental data obtained by Khalifa et al. (2013a) for a parallel triangular array. Downstream the vibrating tube, velocity perturbations were observed to propagate at a speed of about 0.84 times the gap velocity, whereas propagation upstream exhibited a complex pattern. This was attributed to the oscillations induced in the wake of the anterior cylinders, which would behave as secondary perturbation sources.

In the case of the simulations with a 1DOF cylinder developing FEI, the predictions can be considered particularly satisfactory, since the critical velocities estimated under Austermann and Popp's conditions resulted to be just 5-10% below the experimental values in most cases. This capability of the present CFD procedure was then applied to investigate the effect of modifying some parameters of the system. It was found that increasing the pitch ratio from 1.25 to 1.375 resulted in an increment of critical velocity of the order of 10%, with little variation for higher $P/d$ values up to 1.58 (highest $P/d$ tested). Analogously, augmenting the Reynolds number also provoked

the shift of the critical velocity towards higher values. This might suggest defining a limit pitch ratio so that the estimations obtained for that limit pitch ratio and low Reynolds number could be used as reasonable conservative bounds of the instability thresholds for higher tube spacing. On the contrary, arrays with lower tube spacing would require specific estimations of critical velocity.

Finally, the consideration of a second degree of freedom for the flexible tube, thus allowing motion both in the transverse direction and streamwise, showed that the critical velocities reduced by 25-30% though the instability still took place in the transverse direction. According to this, the computations intended to estimate critical velocities for FEI should include two-degree-of-freedom tubes in order to obtain reasonable conservative predictions.

It should be recalled that these conclusions have been derived from numerical tests on a specific configuration (normal triangular array with a single flexible tube) under certain operating conditions. Further research is required to verify whether these conclusions can be extended to other array configurations.

**Acknowledgment**

The authors gratefully acknowledge the financial support of the Principality of Asturias Government under the PhD grant BP-12054 awarded to Ms. de Pedro.

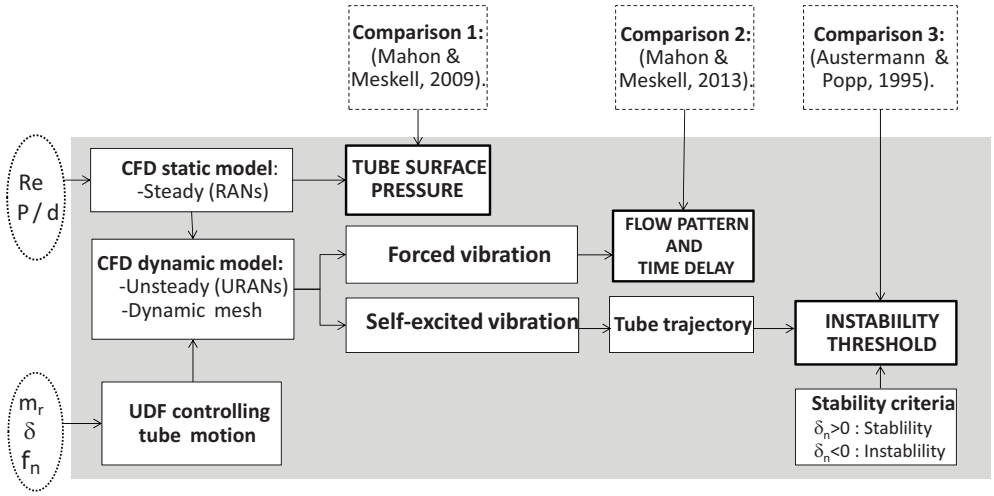


Figure 1: Scheme of CFD simulations and contrast to experimental data.

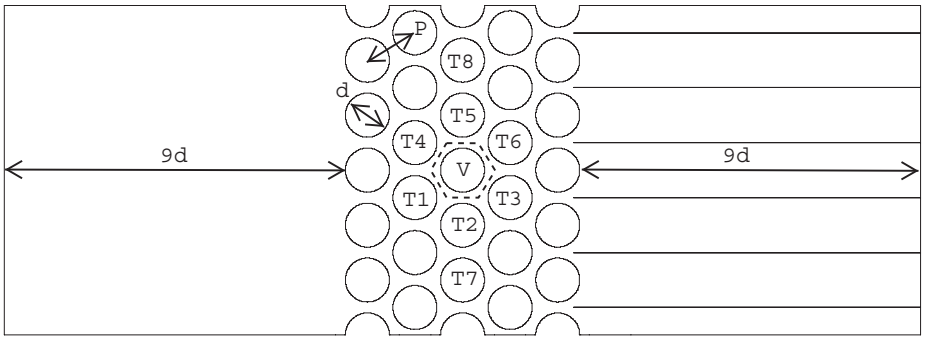


Figure 2: Array configuration and computational domain.

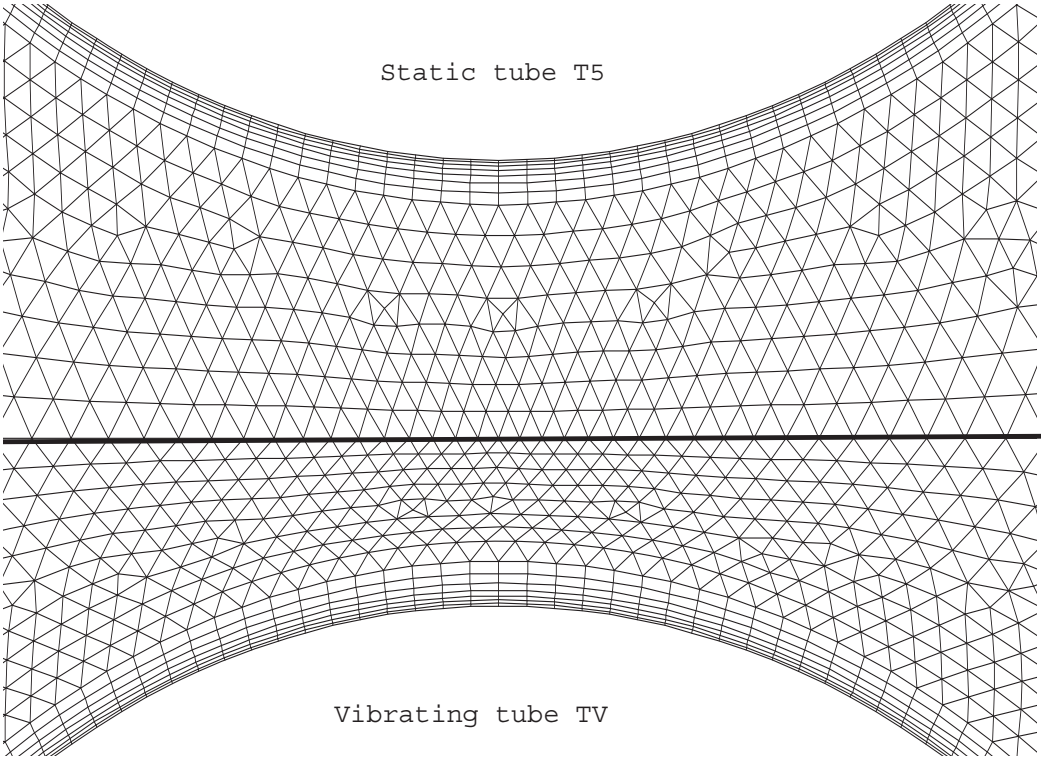


Figure 3: Mesh detail in the region between cylinders T5 (static) and TV (shifted 4% of tube diameter upwards), $P/d$=1.25.

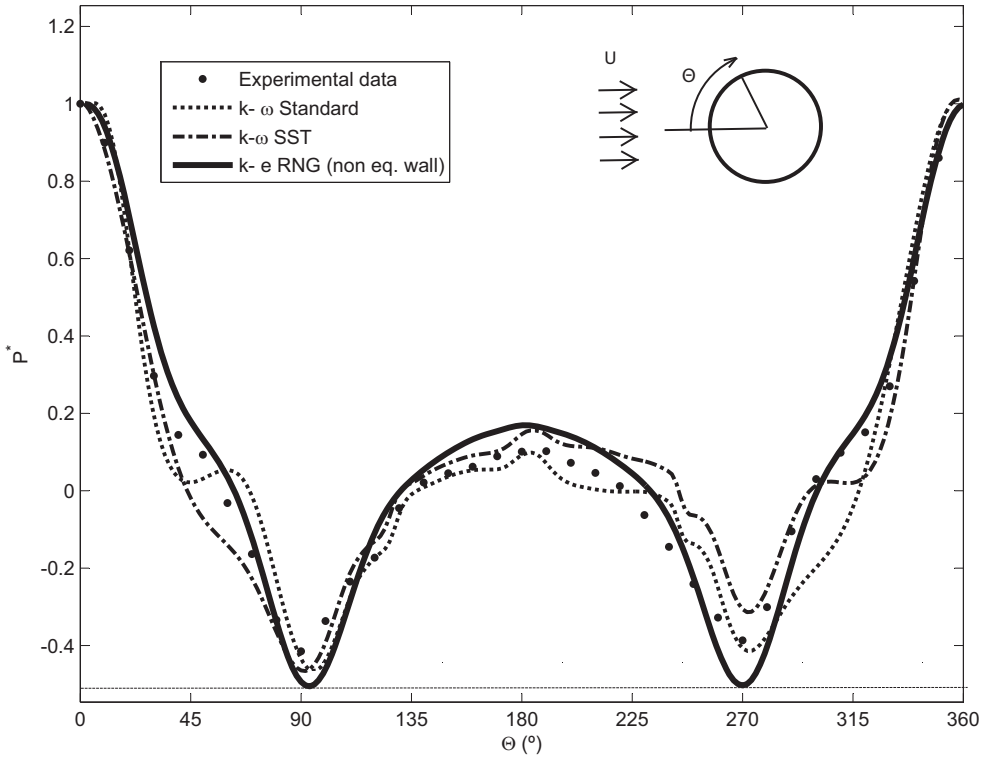


Figure 4: Pressure coefficient computed on tube TV with different turbulence models and Mahon and Meskell's experimental data (2009) .

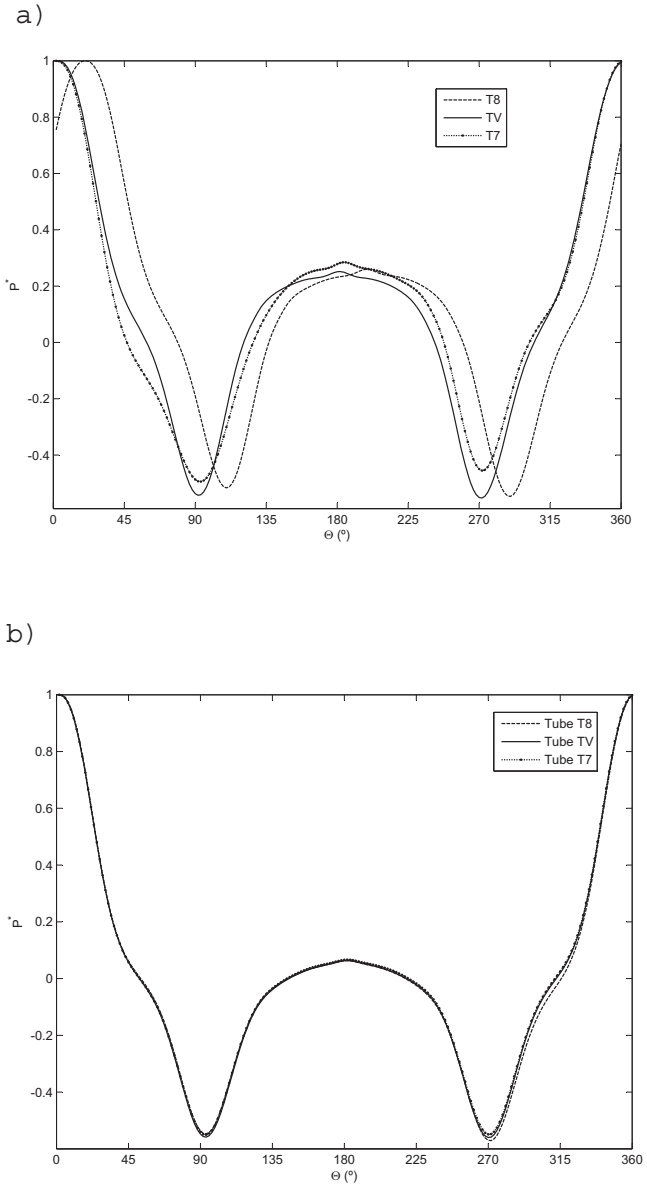


Figure 5: Pressure coefficient on tubes TV, T7 and T8. Boundary conditions at the channel sides downstream the array as (a) full-slip walls, (b) periodic.

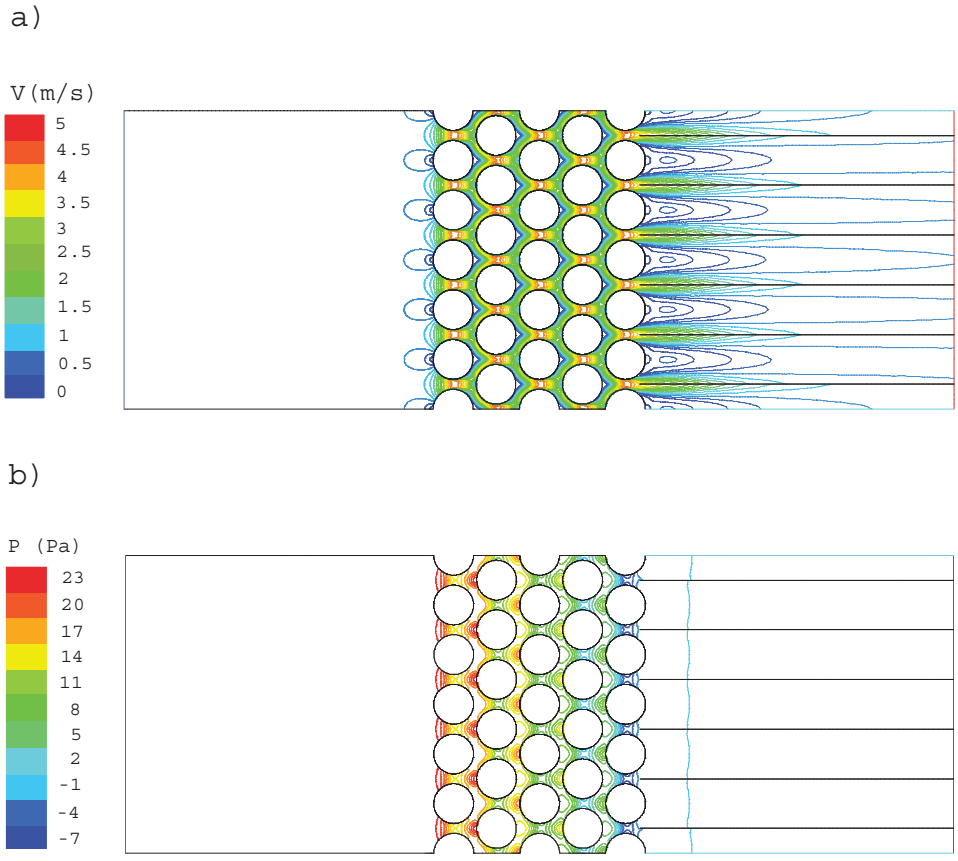


Figure 6: Contours of (a) velocity magnitude and (b) static pressure, computed with the static model ($P/d$=1.25, $U_0$=0.89 m/s) with the $k-\epsilon$-RNG turbulence model and periodic conditions at the channel sides downstream the array.

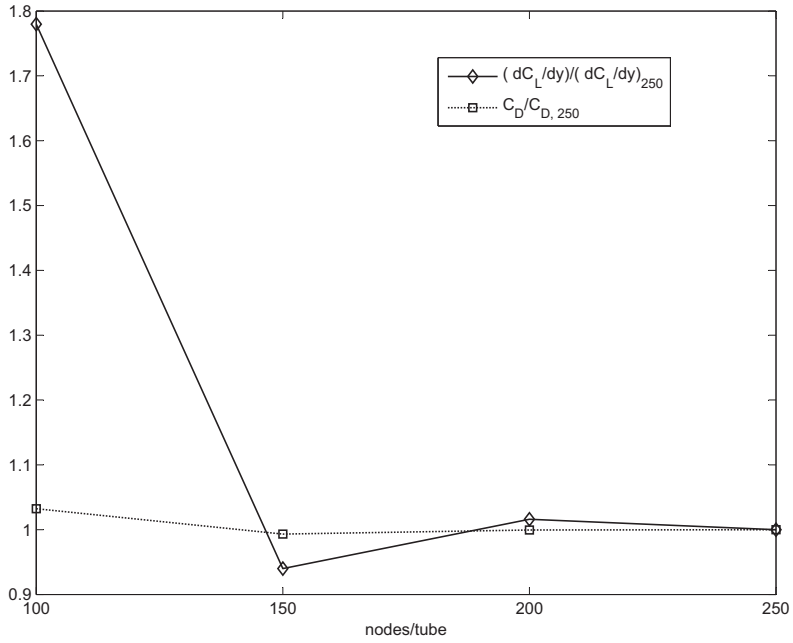


Figure 7: Effect of number of nodes per tube perimeter on predictions of lift coefficient with respect to tube position for tube TV ($P/d$=1.25).

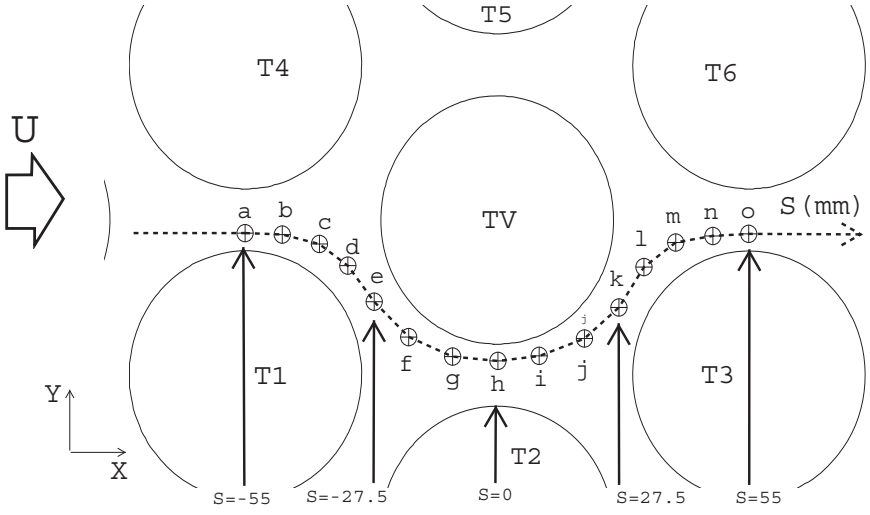


Figure 8: Position of nodes for velocity and pressure monitoring with the tube TV undergoing forced oscillations. S = curvilinear coordinate.

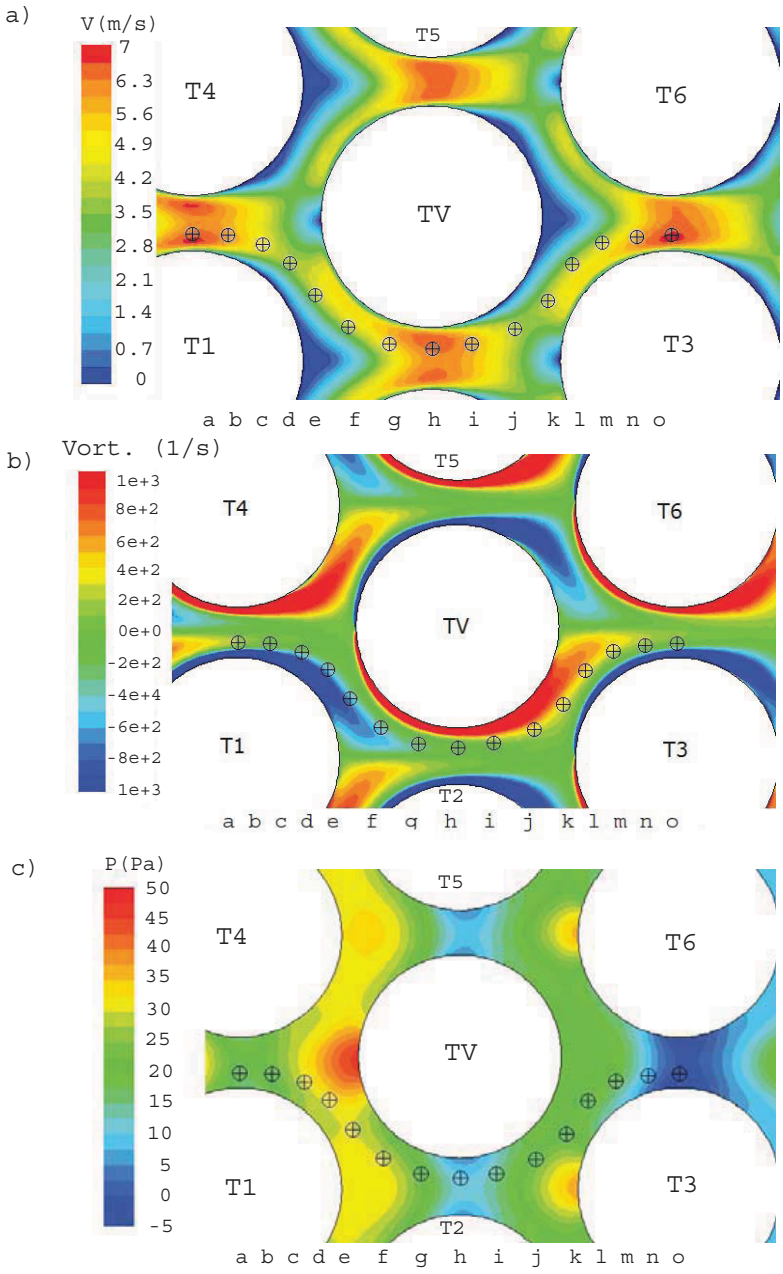


Figure 9: Instantaneous distribution of the (a) velocity magnitude (b) vorticity and (c) static pressure, for $P/d$=1.25 $U_0$=1.26 m/s and tube TV oscillating transversely at 7.8Hz with amplitude of 3% of tube diameter. Image at the instant of maximum displacement upwards.

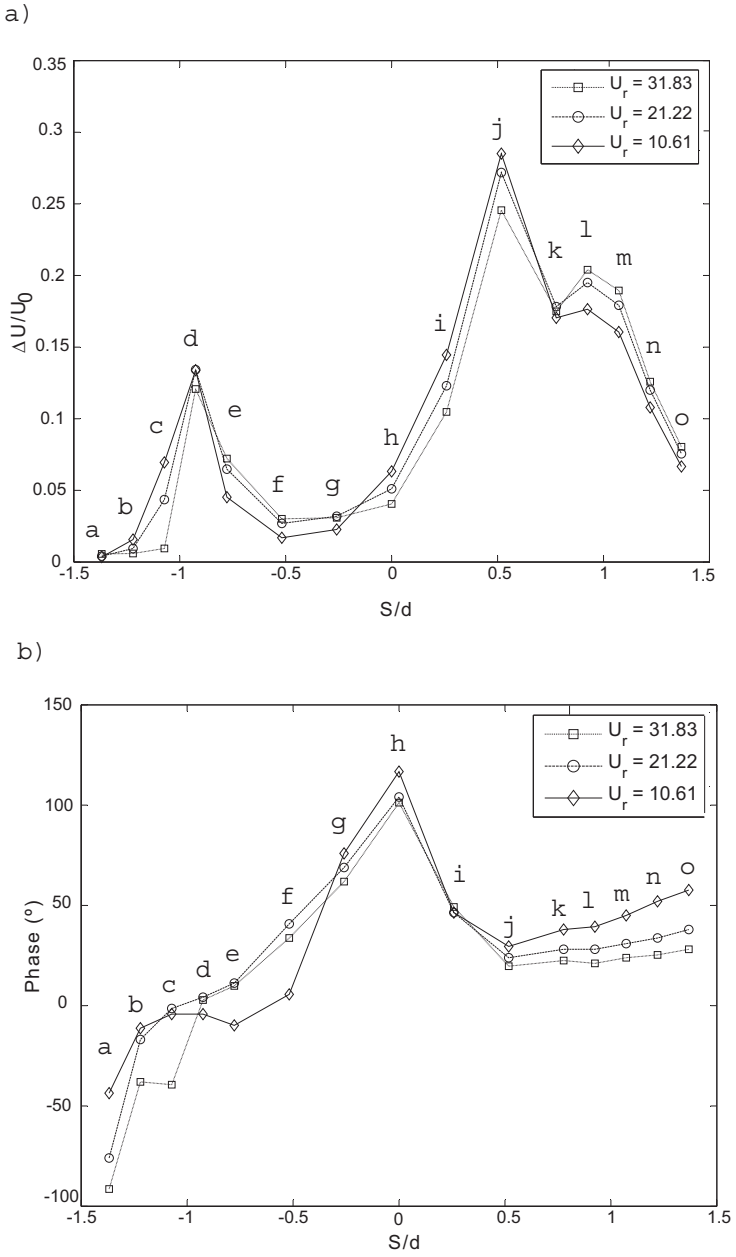


Figure 10: Amplitude and phase lag (relative to tube TV position) of the velocity fluctuation for three reduced velocities, with tube TV oscillating at 7.8Hz and amplitude of 0.01× d, $P/d = 1.25$.

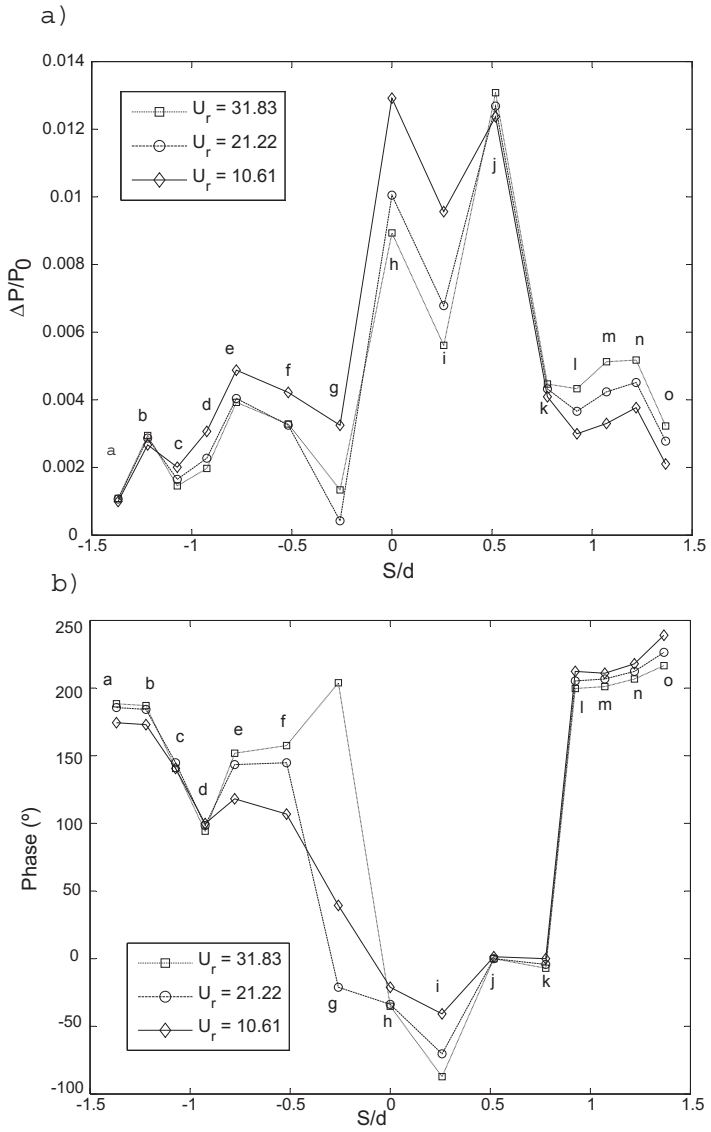


Figure 11: Amplitude and phase lag (relative to tube TV position) of the static pressure. Conditions as in Figure 10.

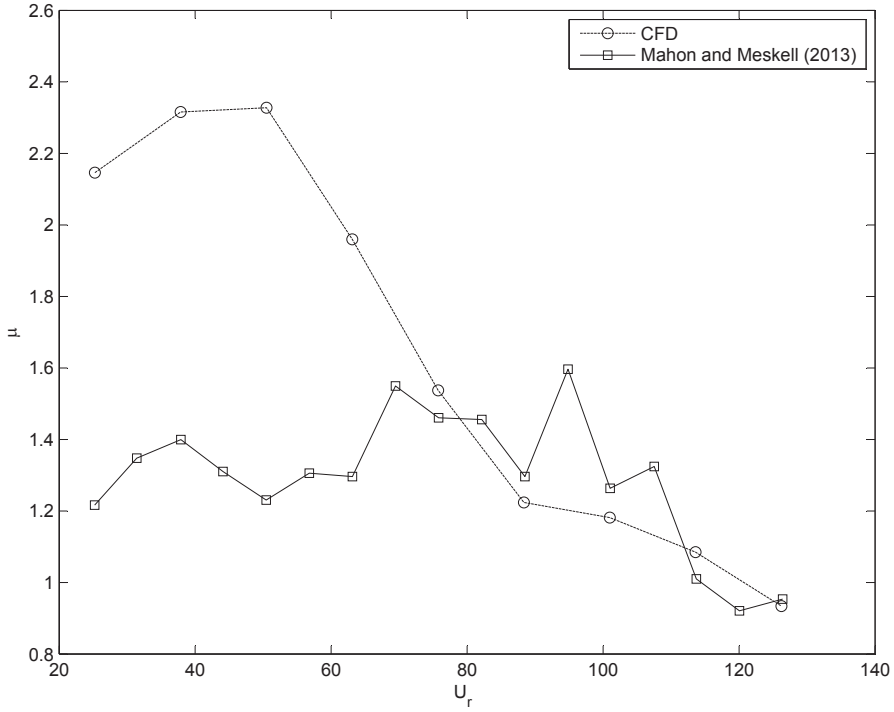


Figure 12: Normalized time lag of the lift coefficient on tube TV as a function of the reduced velocity ($P/d$=1.32, f=8.6 Hz, vibration amplitude = 0.01 $\times$d): current predictions and experimental data of (Mahon and Meskell (2013)).

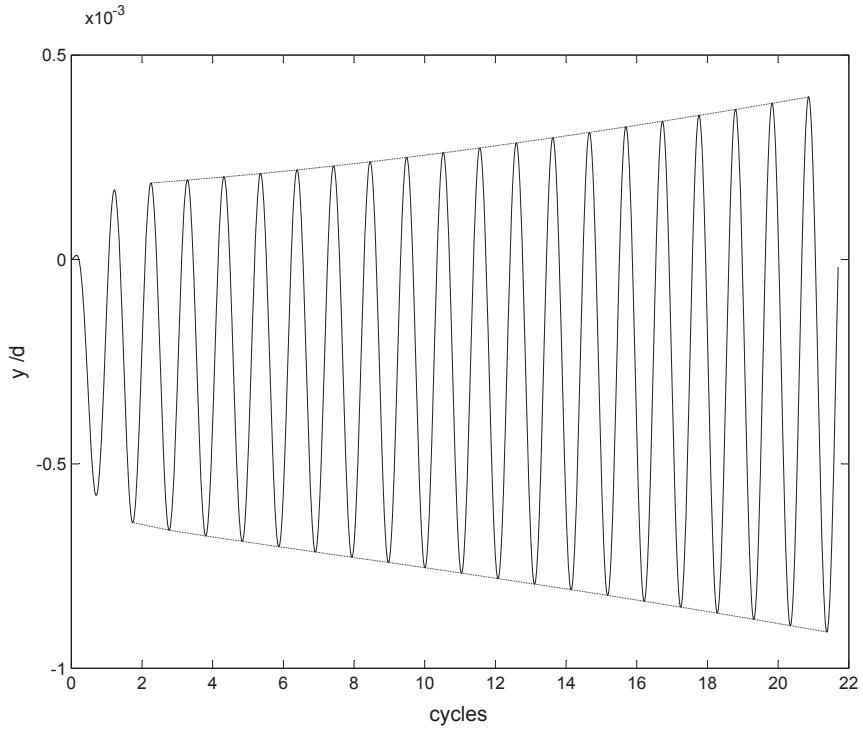


Figure 13: Example of tube response in unstable regime ($P/d = 1.375$, $m_r\delta$=25.17 and $U_0 = 3.44m/s$).

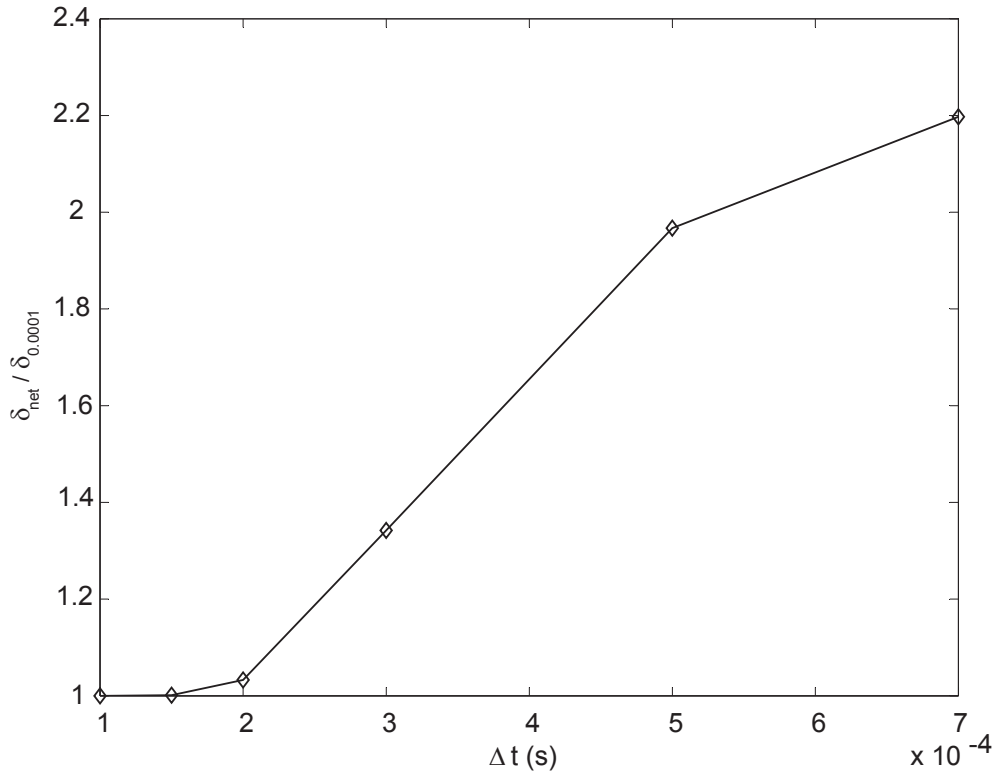


Figure 14: Effect of the time step on the computed damping of the coupled system ($P/d$=1.25, $m_r\delta$=26.7, $U_0$=1.58 and $f_n$=9.42Hz).

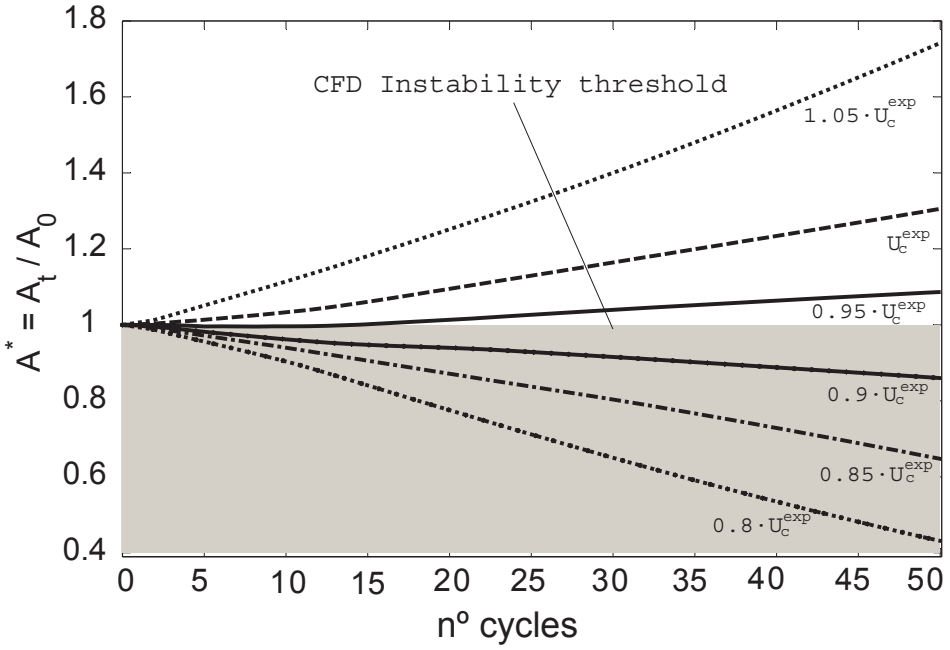


Figure 15: Envelope curves of tube response for cross-flow velocity increasing from stable to unstable regime ($P/d$=1.25,$m_r\delta$=26.7, $U_c^{exp}$=critical velocity determined by Austermann and Popp (1995)).

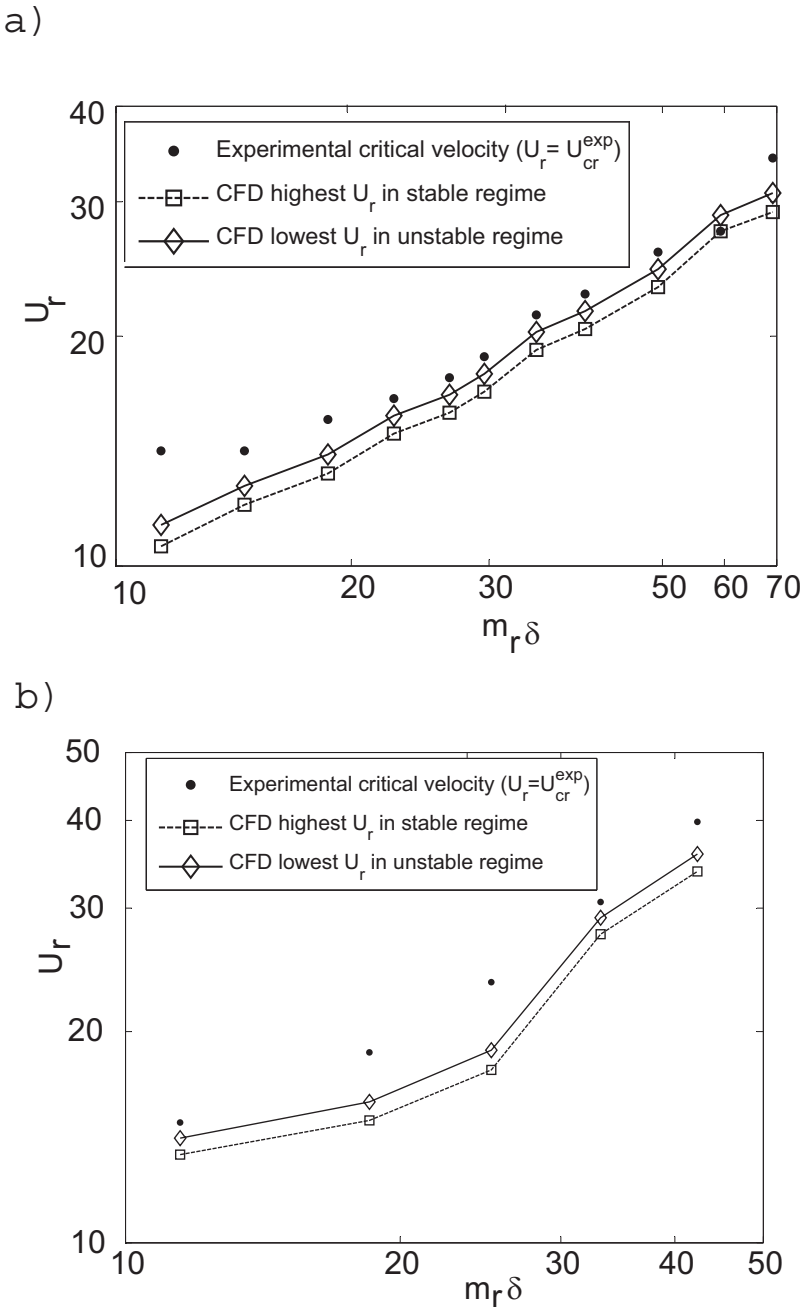


Figure 16: Experimental critical velocity (Austermann and Popp (1995)) and CFD predictions of highest velocity in stable regime and lowest velocity in unstable regime for: (a) $P/d$=1.25, (b) $P/d$=1.375.

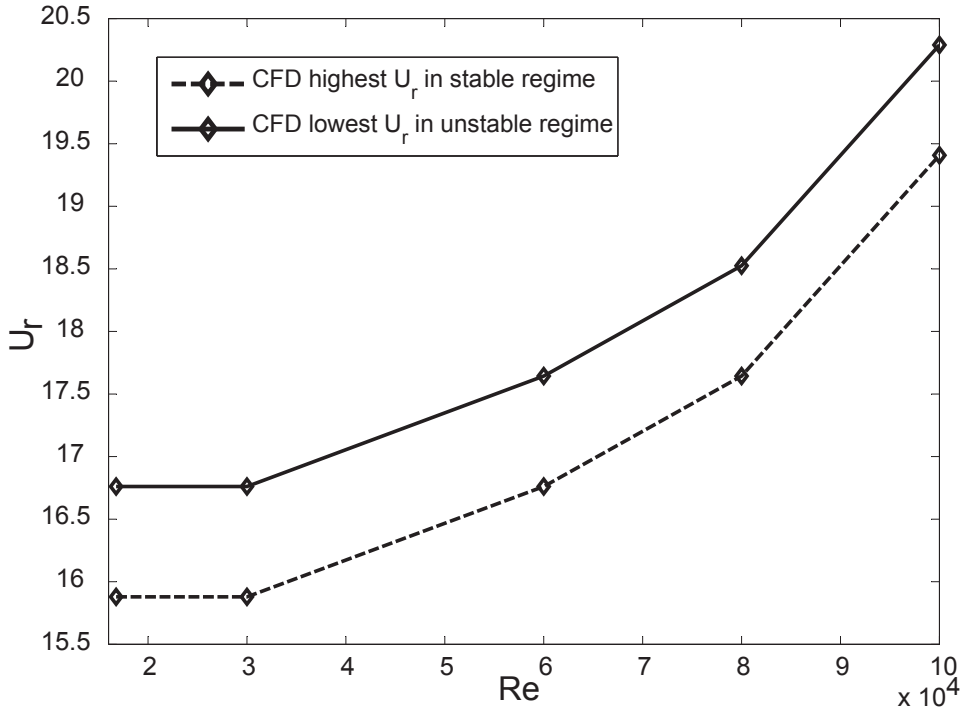


Figure 17: Effect of Reynolds number on the predicted critical velocity ($P/d$=1.25, $m_r\delta$ = 26.7, Re based on gap velocity).

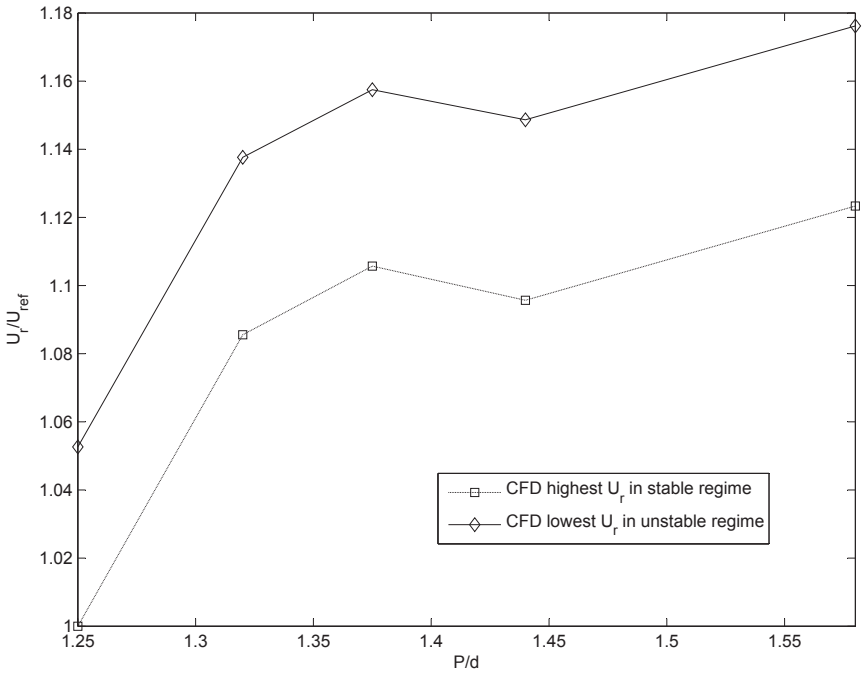


Figure 18: Effect of pitch ratio on the predicted critical velocity ($m_r\delta = 26.7$).

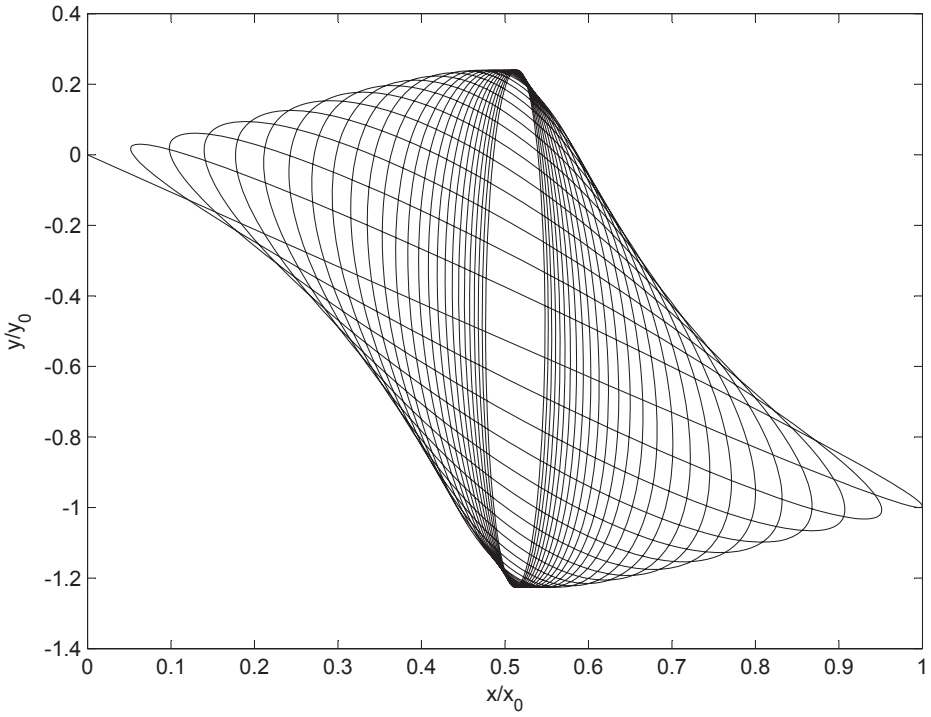


Figure 19: Orbital motion of tube TV with 2 degrees of freedom, showing instability in the transverse direction ($P/d$=1.25, $m_r\delta$=26.7, $U_r$=22.2), $X_0/d$=$8.6\times10^{-3}$, $Y_0/d$=$5.9\times10^{-5}$.

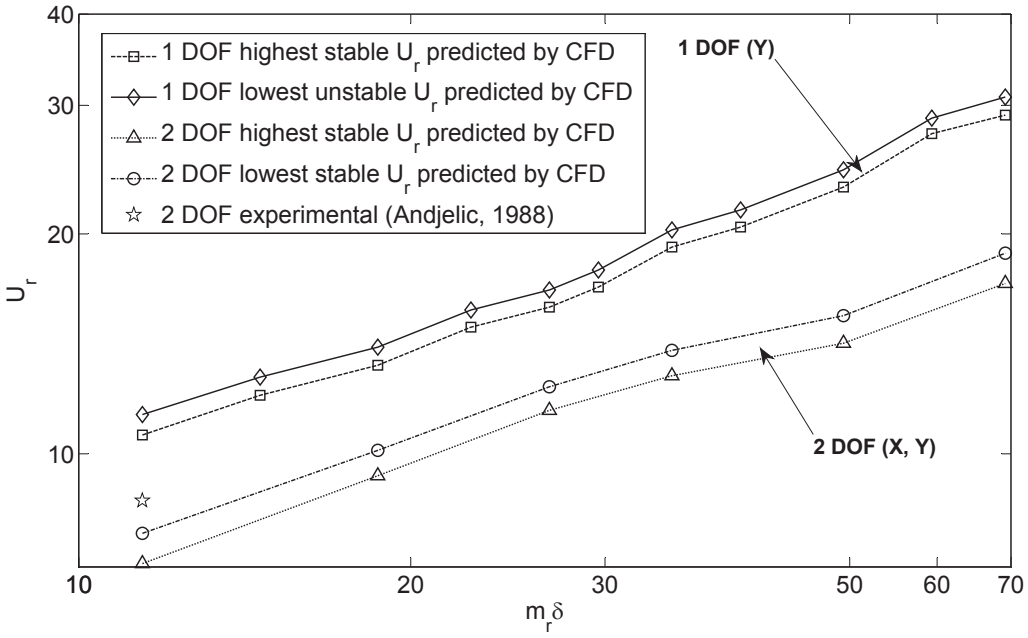


Figure 20: Comparison of instability thresholds obtained for the tube TV oscillating with one degree of freedom (transverse direction Y) and two degrees of freedom (motion with X and Y components).

## References

Anderson, B., Hassan, M., Mohany, A., 2014. Modelling of fluidelastic instability in a square inline tube array including the boundary layer effect. Journal of Fluids and Structures 132, 362–375.

Andjelic, M., 1988. Stabilitatsverhalten querangestromter rohrbundel mit versetzter dreieckteilung. Dissertation, Institute of Mechanics, University of Hannover, Germany.

ANSYS, 2013. Fluent user 's guide.

Au-Yang, M. K., Blevins, R. D., Mulcahy, T. M., 1991. Flow-induced vibration analysis of tube bundlesa proposed, section iii appendix n: Nonmandatory code. Journal of Pressure Vessel Technology 113, 257–267.

Austermann, R., Popp, K., 1995. Stability behaviour of a single flexible cylinder in rigid tube arrays of different geometry subjected to cross-flow. Journal of Fluids and Structures 9 (3), 303 – 322.

Charreton, C., Béguin, C., Yu, K. R., Étienne, S., 2015. Effect of reynolds number on the stability of a single flexible tube predicted by the quasi-steady model in tube bundles. Journal of Fluids and Structures 56, 107–123.

Chen, S. S., 1983a. Instability mechanisms and stability criteria of a group of circular cylinders subjected to cross-flow, part i: Theory. Journal of Vibrations, Acoustics, Stress, Reliability and Design 105, 51–58.

Chen, S. S., 1983b. Instability mechanisms and stability criteria of a group of circular cylinders subjected to cross-flow, part ii: Numerical results and discussion. Journal of Vibrations, Acoustics, Stress, Reliability and Design 105, 253–260.

Chen, S. S., Jendrzjczyk, J. A., 1981. Experiments on fluid instability in tube banks subjected to liquid cross flow. Journal of Sound and Vibration 78, 355–381.

de Paula, A. V., Endres, L. A. M., Moller, S. V., 2012. Bistable features of the turbulent flow in tube banks of triangular arrangement. Nuclear Engineering and Design 249, 379–387.

El Bouzidi, S., Hassan, M., 2015. An investigation of time lag causing fluidelastic instability. Journal of Fluids and Structures 57, 264–276.

Granger, S., Paidoussis, M., 1996. An improvement to the quasi-steady model with application to cross-flow-induced vibration of tube arrays. Journal of Fluid Mechanics 320, 163–184.

Hassan, M., El Bouzidi, S., 2012. Unsteady fluid forces and the time delay in a vibrating tube subjected to cross flow. In Proceedings of the 10th International Conference on Flow-Induced Vibration - FIV 2012 (Eds. G. Bennett and C. Meskell). Dublin, Ireland., 107–114.

Hassan, M., Gerber, A., Omar, H., 2010. Numerical estimation of fluidelastic instability in tube arrays. Journal of Pressure and Vessel Technology 132, 041307.

Iacovides, H., Launder, B., Alastair, W., 2014. A comparison and assessment of approaches for modelling flow over in-line tube banks. International Journal of Heat and Fluid Flow 49, 69–79.

Khalifa, A., Weaver, D., Ziada, S., 2012. A single flexible tube in a rigid array as a model for fluidelastic instability in tube bundles. Journal of Fluids and Structures 34, 14–32.

Khalifa, A., Weaver, D., Ziada, S., 2013a. An experimental study of flow-induced vibration and the associated flow perturbations in a parallel triangular tube array. Journal of Pressure Vessel Technology 135, 030904.

Khalifa, A., Weaver, D., Ziada, S., 2013b. Modeling of the phase lag causing fluidelastic instability in a parallel triangular tube array. Journal of Fluids and Structures 43, 371–384.

Lever, J., Weaver, D., 1986a. On the stability of heat exchanger tube bundles, part i: modified theoretical model. Journal of Sound and Vibration 107, 375–392.

Lever, J., Weaver, D., 1986b. On the stability of heat exchanger tube bundles, part ii: Numerical results and comparison with experiments. Journal of Sound and Vibration 107, 393–410.

Mahon, J., Meskell, C., 2009. Surface pressure distribution survey in normal triangular tube arrays. journal of fluids and structures. Journal of Fluids and Structures 25, 1348–1368.

Mahon, J., Meskell, C., 2013. Estimation of the time delay associated with

damping controlled fluidelastic instability in a normal triangular tube array. Journal of Pressure Vessel Technology 135, 030903.

Meskell, C., Fitzpatrick, J. A., 2003. Investigation of nonlinear behaviour of damping controlled fluidelastic instability in a normal triangular tube array. Journal of Fluids and Structures 18, 573–593.

Mewes, D., Stockmeier, D., 1991. A new model for damping controlled fluidelastic instability in heat exchanger tube arrays. In Flow Induced Vibrations, 231–242.

Olinto, C. R., Indrusiak, M. L. S., Endres, L. A. M., Moller, S. V., 2009. Experimental study of the characteristics of the flow in the first rows of tube banks. Nuclear Engineering and Design 239, 2022–2034.

Paidoussis, M. P., Price, S. J., 1988. The mechanisms underlying flow-induced instabilities of cylinder arrays in crossflow. Journal of Fluid Mechanics 187, 45–59.

Pettigrew, M. J., Taylor, C. E., 2003a. Vibration analysis of shell and tube heat exchangers, an overview-part i: flow, damping, fluidelastic instability. Journal of Fluids and Structures 18, 469–483.

Pettigrew, M. J., Taylor, C. E., 2003b. Vibration analysis of shell and tube heat exchangers, an overview-part ii: vibration response, fretting-wear, guidelines. Journal of Fluids and Structures 18, 485–500.

Price, S. J., 1995. A review of theoretical models for fluidelastic instability of cylinder arrays in cross-flow. Journal of Fluids and Structures 9, 463–518.

Price, S. J., Paidoussis, M. P., 1984. An improved mathematical model for the stability of cylinder rows subject to cross-flow. Journal of Sound and Vibration 97, 615–640.

Sawadogo, T., Mureithi, N., 2013. Time domain simulation of the vibration of a steam generator tube subjected to fluidelastic forces induced by two-phase cross-flow. Journal of Pressure Vessel Technology 135, 030905.

Scott, P., 1987. Flow visualization of cross-flow induced vibrations in tubearrays. Masters Thesis. McMaster University, Hamilton, Ontario, Canada.

Weaver, D. S., Fitzpatrick, J. A., 1988. A review of cross-flow induced vibrations in heat exchanger tube arrays. Journal of Fluids and Structures 2, 73–93.

Yetisir, M., Weaver, D. S., 1993a. An unsteady theory for fluidelastic instability in an array of flexible tubes in cross-flow. part i: Theory. Journal of Fluids and Structures 7, 751–766.

Yetisir, M., Weaver, D. S., 1993b. An unsteady theory for fluidelastic instability in an array of flexible tubes in cross-flow. part ii: Results and comparison with experiments. Journal of Fluids and Structures 7, 767–782.